Acta Materialia 275 (2024) 120055

Contents lists available at ScienceDirect

Acta Materialia

journal homepage: www.elsevier.com/locate/actamat

Microstructure and properties of high-entropy-superalloy microlattices fabricated by direct ink writing

Ming Chen *, Dingchang Zhang, Ya-Chu Hsu, David C. Dunand

Department of Materials Science & Engineering, Northwestern University, Evanston IL, USA

ARTICLE INFO

Keywords:
Direct ink writing
High entropy superalloy
Microstructural engineering
Architected structures
High-temperature strength

ABSTRACT

Ni-Co-Fe-based high-entropy superalloys (HESAs) are fabricated into microlattices *via* a three-step process: (i) layer-by-layer extrusion of inks containing elemental powders (Ni, Co, Fe, Cr, Ti) and $TiAl_3$ powders; (ii) sintering to densify and homogenize the struts; (iii) aging to achieve a γ/γ' microstructure. The struts of the microlattices show a nearly pore-free and fully-homogenized microstructure. Increasing the Ti concentration from 4 at% ($Al_9Co_{26}Cr_7Fe_{16}Ni_{38}Ti_4$) to 9 at% ($Al_8Co_{25}Cr_7Fe_{15}Ni_{36}Ti_9$) leads to a significant increase in the volume fraction of strengthening γ' precipitates, from 51 to 78 %. Furthermore, in the Ti-rich composition, the γ' precipitates exhibit a sharp-edged cubic morphology with larger sizes and higher lattice misfit (0.63 %) with respect to the γ matrix. As a result, Ti-rich HESA microlattices show higher strength at ambient temperature than Ti-poor ones, while retaining high compressive ductility (> 60 %). They also demonstrate superior specific strengths when compared to bulk Inconel 617 and other representative bulk HESA, up to 1000 °C. The combination of low-density (2.29–3.15 g/cm^3), high strength at elevated temperatures, and high processability positions HESA microlattices from direct ink writing as promising candidates for structural components in extreme operating conditions. The versatility of the process is demonstrated by printing and sintering three miniature HESA objects with complex shapes (hollow turbine blade, gyroid heat exchanger, and compressor wheel).

1. Introduction

High-entropy alloys (HEAs) represent a large class of alloys consisting of five or more principal elements with each concentration in a range of 5–35 at% [1,2], with microstructures and phase components tailored to achieve a desirable combination of enhanced strength, microstructure stability, creep resistance, and oxidation resistance (for high-temperature applications) [3–5]. Equiatomic CoCrFeMnNi (the Cantor alloy) has a single face-centered-cubic (FCC) phase [6] and can be modified: for example, adding V and decreasing the Co concentration to 5 or 10 at% induces precipitation of the sigma phase during the post annealing to increase high-temperature strengths [7,8]. Removing Mn and adding Al lead to the $Al_xCoCrFeNi$-based HEA family, which has received considerable attention given their tunable phase compositions which transition from face-centered cubic (FCC) to body-centered cubic (BCC) dominant structure with increasing Al concentration [9,10]. By adding Cu or Ti to $Al_xCoCrFeNi$-based alloys ($0 < x < 0.3$) with a single FCC phase [11–16], γ/γ' microstructures similar to those achieved in Ni- or Co-based superalloys are attained. High-entropy superalloys (HESAs) refer to multi-principal elemental compositions based on Co, Cr, Fe, and Ni, with minor or no addition of refractory elements, which exhibit a γ/γ' microstructure and aim to achieve a balance between high-temperature strength, creep resistance, and oxidation resistance, thereby surpassing the performance of conventional superalloys [4,17]. In addition, HESAs also show enhanced microstructural stability at high temperatures due to sluggish diffusion kinetics [18,19], as compared to conventional Ni-based superalloys. In particular, the $Al_{10}Co_{25}Cr_8Fe_{15}Ni_{36}Ti_6$ alloy encompassing the dominant γ/γ' microstructure and a minor Heusler phase shows a combination of high strength, creep resistance, and oxidation resistance at 1000 °C *via* tuning of the Al concentration [20,21].

The rapid development of additive manufacturing (AM) facilitates scalable manufacturing of superalloys [22,23], the Cantor alloy [24], $Al_xCoCrFeNi$-based alloys [25,26], and refractory HEAs [27–29]; most AM research uses beam-based technologies where powders are melted, e.g., laser powder bed fusion (L-PBF), electron-beam selective melting (E-SM), and direct energy deposition (DED) [30]. These processes achieve rapid heating and cooling (e.g., 10^4–10^6 K/s in L-PBF [31,32], 5 ×

* Corresponding author.
E-mail address: ming.chen@northwestern.edu (M. Chen).

https://doi.org/10.1016/j.actamat.2024.120055
Received 10 January 2024; Received in revised form 2 April 2024; Accepted 27 May 2024
Available online 28 May 2024

10^4 K/s in E-SM [33,34], and $1 \times 10^3 - 3 \times 10^4$ K/s in DED [35,36]), often resulting in residual stresses and epitaxial growth of column grains with anisotropic properties, which deteriorate strength, fatigue resistance, and fracture toughness [37,38]. The deleterious effect of columnar grains on strength is reduced in titanium alloys, e.g., Ti6Al4V, which achieve high strengths due to the formation of fine martensitic phase (α') induced by rapid cooling during beam-based 3D printing [39,40]. In addition, residual stresses can induce cracking, particularly in hard and brittle metals. This issue can be mitigated by optimizing processing parameters (e.g., during E-SM processing of γ-TiAl intermetallic compounds [41]), or by adding nanoparticles to control solidification and alter grain structures in the Cantor alloy [42]. Nevertheless, many superalloys and HESA are still prone to cracking in beam-based additive manufacturing due to poor weldability given their highly alloyed nature and the high volume fraction of strengthening γ' precipitates [22,43,44].

Direct ink writing (DIW) based 3D printing represents an alternative AM method to produce objects with intricate structures in three steps [45]: (i) green specimens are fabricated at ambient temperature layer-by-layer, by depositing extruded inks containing metallic powders (in elemental or pre-alloyed form); (ii) the green specimens are thermally treated to remove organic solvents and binders; and (iii) the powders are densified by sintering while also achieving homogenization by interdiffusion. The alloy is never melted, thus avoiding texture and segregation associated with the fusion-solidification process prevalent in beam-based AM. Also, the isothermal sintering and homogenization conditions and the slow, uniform subsequent cooling minimize residual stresses which often lead to cracking in beam-based AM processes subjected to very high thermal gradients [46,47]. Moreover, various powder precursors (e.g., metals, oxides, and hydrides) can be utilized for ink preparation, with a wide range of diameters (from tenths to tens of microns) and irregular shapes, which are unsuitable for powder bed methods where good flowability is necessary [19,48–53]. Using elemental powders, DIW was performed for metals (e.g., Mg [54], Cu [55], and Ti [56]), binary alloys (e.g., Fe-Ni [19] and NiTi [57]), and multi-element alloys: Heusler and half-Heusler alloys (e.g., Ni-Mn-Ga [58] and Ti-Ni-Sn [59]) and Co-Ni-W-Al superalloys [60]. Pre-alloyed metallic powders were used to fabricate alloyed steels [61,62], half-Heusler alloys NbCoSb [63], and HEA CoCrFeMnNi microlattices [64]. However, the synthesis of pre-alloyed powders is an energy-intensive and high-cost process, particularly for HEAs with multiple principal elements and designed compositions. To reduce cost, and time and simplify precursors preparation, oxide powders were utilized in DIW and then reduced by H_2 to synthesize elemental metals (e.g., Ag [65], Fe, and Ni [45,50]), steels [66], and equiatomic HEA (CoCrFeNi [67], CoCrCuFeNi [68], and CoCrFeMnNi [69,70]).

In this study, we fabricate HESA microlattices with nominal $Al_{10}Co_{25}Cr_8Fe_{15}Ni_{36}Ti_6$ composition and γ/γ' microstructures to achieve high strengths at elevated temperatures, using 3D extrusion and sintering of inks containing a blend of elemental powders (Cr, Ti, Fe, Ni, and Co) and binary $TiAl_3$ powders. This method sidesteps the gas atomization of fully pre-alloyed powders, allowing a very wide range of HESA compositions. The Ti concentration of the above alloy is raised to increase the volume fraction of γ' precipitates and to modify their morphology. Compressive strength and microhardness at ambient temperatures are measured for lattices with various compositions and microstructures. Also, the strength of HESA lattices is measured up to 1000 °C and compared with other HEAs and superalloys. Finally, miniature objects with complex architectures (turbine blades, gyroid heat exchanger, and compressor wheels) are printed and sintered to demonstrate the versatility of this manufacturing method.

2. Materials and methods

2.1. Ink preparation, direct ink writing (DIW), and sintering

The process, from ink preparation to DIW and sintering, is depicted schematically in Fig. 1a. Six powders with spherical and irregular shapes (Supplementary Fig. S1) were used: $TiAl_3$ (44 μm, ≥99.5 %, ThermoFisher Scientific), Co (2 μm, 99.8 %, Sigma-Aldrich), Cr (10 μm, 99.98 %, Nanografi Nano Technology), Fe (5 μm, 99.99 %, Nanografi Nano Technology), Ni (5 μm, 99.5 %, US Nano) and Ti powders (0–25 μm, 99.79 %, AP&C Powder Metallurgy). The irregular morphologies of some of the powders are expected to enhance the interlocking between particles and prevent fracture of the green bodies after the debinding process [71]. Inks were prepared by combining the powders with dibutyl phthalate (DBP, 0.45 g/cm^3, Sigma-Aldrich) as a plasticizer to improve the flow of the slurry, ethylene glycol butyl ether (EGBE, 0.9 g/cm^3, Sigma-Aldrich) as a surfactant to promote particles dispersion in the slurry, polystyrene (PS, Sigma-Aldrich) as binder, and anhydrous dichloromethane (DCM, Sigma-Aldrich) as solvent, in two steps. In the first step, the metallic powders (with a total volume of 4 cm^3) mixed with 1.8 g of EGBE and 12 mL of DCM, were loaded within an Ar glovebox into an air-tight PET bottle for wet milling in a roller mixer with a rotational speed of 80 rpm for 4 h, using 60 g of yttria-stabilized zirconia balls. In the second step, 0.3 g of DBP, 1.32 g of PS, and 18 mL of DCM were added into the bottle in an Ar glovebox, and mixing in a roller mixer (80 rpm) was performed again for 4 h. $TiAl_3$ powders (melting point: T_m=1340 °C [72]) were utilized instead of Al powders (T_m=662 °C), to suppress Al loss due to evaporation during high-temperature sintering.

Based on the original (nominal) $Al_{10}Co_{25}Cr_8Fe_{15}Ni_{36}Ti_6$ composition of the first HESA, a second alloy with a higher Ti concentration (9 vs. 4 at %) was printed by adjusting the amounts of powder feedstocks in the ink. The compositions of the low- and high-Ti HESA are listed in Table 1, as measured by EDS on several regions of a large cross-section of microlattices and then averaged for each sample.

The inks were heated to 55 °C to evaporate DCM and achieve a viscosity sufficiently low to allow ink extrusion from the conical nozzle at high shear rates, but sufficiently high to prevent sagging at low shear rates under gravity after deposition [48] (the rheological properties of the DCM-DBP-PS ink system were characterized and reported in Ref [73]. The DIW-based 3D printing was conducted with a 3D-Bioplotter (Envision TEC, Germany) with tapered polyethylene nozzles (with 410 μm tip opening, Nordson EFD). The orthogonal microlattices, with overall dimensions $9 \times 9 \times 13.5$ mm^3, were printed with a vertical layer thickness of 330 μm, a horizontal spacing of 1.125 mm between each strut, and a rotation angle of 90° between layers, as shown in Fig. 1a. This lattice structure is suitable for continuous extrusion of a single filament creating a 3D structure without support structures. To further demonstrate the capability of DIW, three miniature objects with complex geometries were printed, as shown in Fig. 1b. Green bodies were dried overnight and then sintered in three steps: (i) evaporation of residual DCM and decomposition of PS at 400 °C for 1.5 h and at 550 °C for 4 h under flowing ultra-high purity (UHP) Ar (99.999 %) to remove organic materials in inks; (ii) sintering at 1220 °C for 20 h in quartz capsules (20 kPa, UHP Ar) and; (iii) aging at 850 °C for 50 h in the same quartz capsules to precipitate the γ' phase.

To smooth their surfaces, the sintered demonstration objects were blasted for 15 or 60 s with glass beads (74–177 μm, Potters) in a sandblaster (Media Blast & Abrasive) using a pressure of 345 kPa. After sandblasting, the surface roughness, Ra (arithmetic mean deviation), was measured at three different regions on struts, using a 3D laser confocal microscope (LEXT OLS5100, Olympus) equipped with a MPLAPON50xLEXT objective. A 200 μm threshold was set between roughness and waviness components.

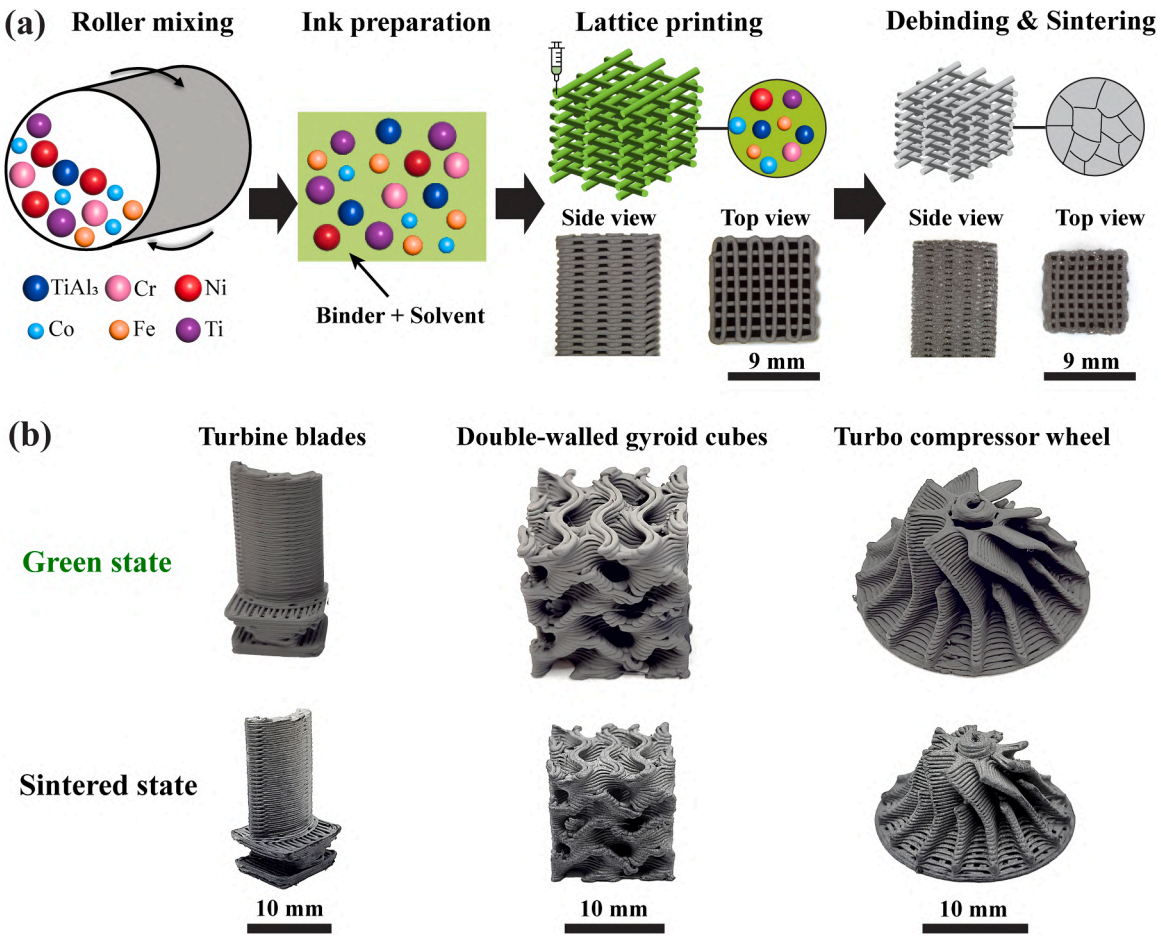

Fig. 1. (a) Schematics of 3D direct ink writing of microlattices. (b) Photographs of miniature turbine blade (with hollow core containing a lattice), double-walled-gyroid cube (for heat exchanger), and compressor wheel after 3D ink printing: (top row) before sintering, in the green state; (bottom row) after sintering, in the densified state, illustrating uniform shrinkage without warping or cracking.

Table 1
. Chemical composition of low-Ti and high-Ti alloys.

Composition		Ni	Co	Fe	Cr	Al	Ti
Nominal $Al_{10}Co_{25}Cr_8Fe_{15}Ni_{36}Ti_6$	wt%	39.1	27.3	15.5	7.7	5.0	5.3
	at%	36.0	25.0	15.0	8.0	10.0	6.0
Low-Ti alloy $Al_9Co_{26}Cr_7Fe_{16}Ni_{38}Ti_4$	wt%	41.2±1.7	27.6±1.3	16.4±3.1	6.8±1.3	4.4±1.0	3.7±1.9
	at%	38.3±1.6	25.5±1.2	16.0±3.0	7.1±1.4	8.9±2.1	4.3±2.2
High-Ti alloy $Al_8Co_{25}Cr_7Fe_{15}Ni_{36}Ti_9$	wt%	38.4±0.9	26.9±1.2	15.7±2.3	6.9±2.7	3.9±0.6	8.2±1.4
	at%	35.6±0.8	24.9±1.1	15.3±2.2	7.2±2.8	7.8±1.3	9.3±1.6

2.2. Materials characterization

Sintered samples were cold-mounted with epoxy resin (Epothin 2 Resin, Buehler), cured for 24 h, and polished with a diamond suspension (MetaDi, Buehler) down to 0.25 μm. The polished surface was then etched with Carapella's reagent for 10–15 s to help image the γ' precipitates. Specimens were coated with a 6 nm thick osmium conductive layer and examined by scanning electron microscopy (SEM) using a Quanta 650 ESEM (ThermoFisher Scientific) instrument equipped with an Oxford AZtec detector for energy dispersive X-ray spectroscopy (EDS). Phases of sintered lattices were identified *via* X-ray diffraction (XRD) in reflection mode with pure Cu Kα1 radiation source in Smartlab 3 kW Gen2. The 2θ reflection angles were scanned in the range of 25–70° at a scanning speed of 2°/min.

2.3. Mechanical testing

Vickers microhardness was measured with a Wilson VH3100 Automated Micro-hardness Tester (Buehler) by averaging values for 10 indents, applying a 0.98 N force for 10 s. The compression tests were performed on lattices at a strain rate of 1.2×10^{-3} s^{-1} on a MTS-5 servo-hydraulic tester with a 100 kN load cell, using oil-lubricated platens; tests were carried out at ambient temperature in air, and also at 700, 800, 900, and 1000 °C under UHP Ar (99.999 %), using titanium shim stock as an oxygen getter. For each temperature, three microlattices were tested. These mechanical experiments were carried out on microlattices which were lightly ground with SiC sandpaper to flatten their top and bottom surfaces.

3. Results and discussion

3.1. Direct ink writing and sintering

Given the excellent mechanical properties of superalloys at elevated temperatures, three printed and sintered miniature objects were chosen to be relevant to high-temperature applications, as shown in Fig. 1b: (i) a turbine blade with 18.7±0.1 mm height and 2.4±0.1 mm blade thickness (hollow with an inner lattice) [74], (ii) a double-walled-gyroid cube for a heat exchanger [75], with 12.4±0.2 mm edge length and 1.0±0.1 mm wall thickness, and (iii) a turbo compressor wheel with 20.0±0.1 mm diameter and 0.8±0.1 mm wall thickness. The objects show high volumetric shrinkage after sintering, as expected, but they maintain their original shape and architecture without any visible distortion or cracks.

To shed light on the microstructural evolution during processing, the microlattices were imaged *via* SEM at different stages of the process. After debinding and pre-sintering, a homogeneous distribution of porosity was observed in the struts, as illustrated on a cross-section of a lattice shown in Fig. 2a. The magnified view in Fig. 2b displays a highly porous structure, as expected from the limited interdiffusion between particles at a relatively low temperature (550 °C) as compared to the melting point of the powders. The EDS maps (Fig. 2c–h) show a uniform distribution of the six elements, without local particle agglomeration or settling, indicating a homogenous mixture of the six powders after wet milling and printing. This uniform distribution of powder is essential for the homogenization of the alloy during the subsequent sintering step, especially given the slow atomic diffusion in high-entropy alloys [76, 77]. Since $TiAl_3$ particles were used as powder precursors, the distribution of Al is correlated with Ti in EDS maps (marked with yellow arrows).

The heat treatments used here to homogenize elements and precipitate the γ' phase were adopted from the literature [20] for bulk specimens with a nominal composition of $Al_{10}Co_{25}Cr_8Fe_{15}Ni_{36}Ti_6$. This also provides a direct comparison of mechanical properties between bulk and microlattice specimens. The microlattices were sintered at 1220 °C for 20 h to densify their struts, and subsequently aged at 850 °C for 50 h to precipitate the γ' strengthening phase. A low-magnification view of a lattice cross-section (Fig. 3a) shows that struts are nearly fully dense, with an average density of 98±1 % as measured at ten different areas using ImageJ analysis. Compared to the green bodies, sintered lattices exhibit a volumetric shrinkage of 57±2 % overall. This volumetric shrinkage may vary somewhat between objects with different shapes and geometries. The specific values of volumetric shrinkage in each specimen could be determined accurately by measuring the geometries before and after heat treatments, enabling precise control of the final specimens after the annealing step to achieve the designed geometries. Densification of the struts is critical to achieve high lattice strengths and

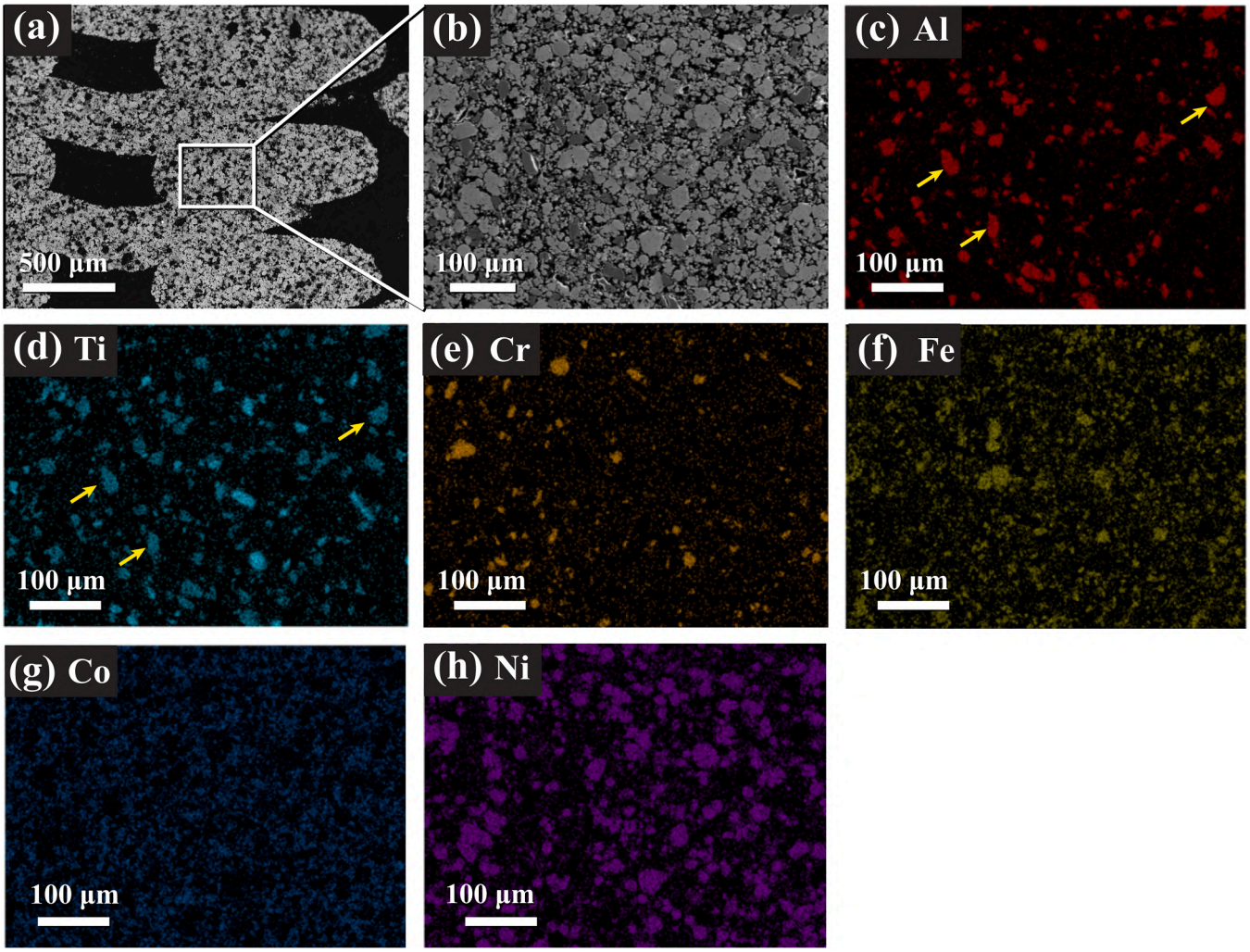

Fig. 2. Cross-sections of a microlattice after debinding (400 °C/1.5 h) and pre-sintering (550 °C/4 h). (a) Secondary electron (SE) micrograph at a low-magnification showing struts and channels (filled with black epoxy). (b) Higher-magnification view of particles in a strut. (c-h) Energy-dispersive X-ray spectroscopy (EDS) maps of elemental distributions in magnified view (b). $TiAl_3$ particles are marked with yellow arrows.

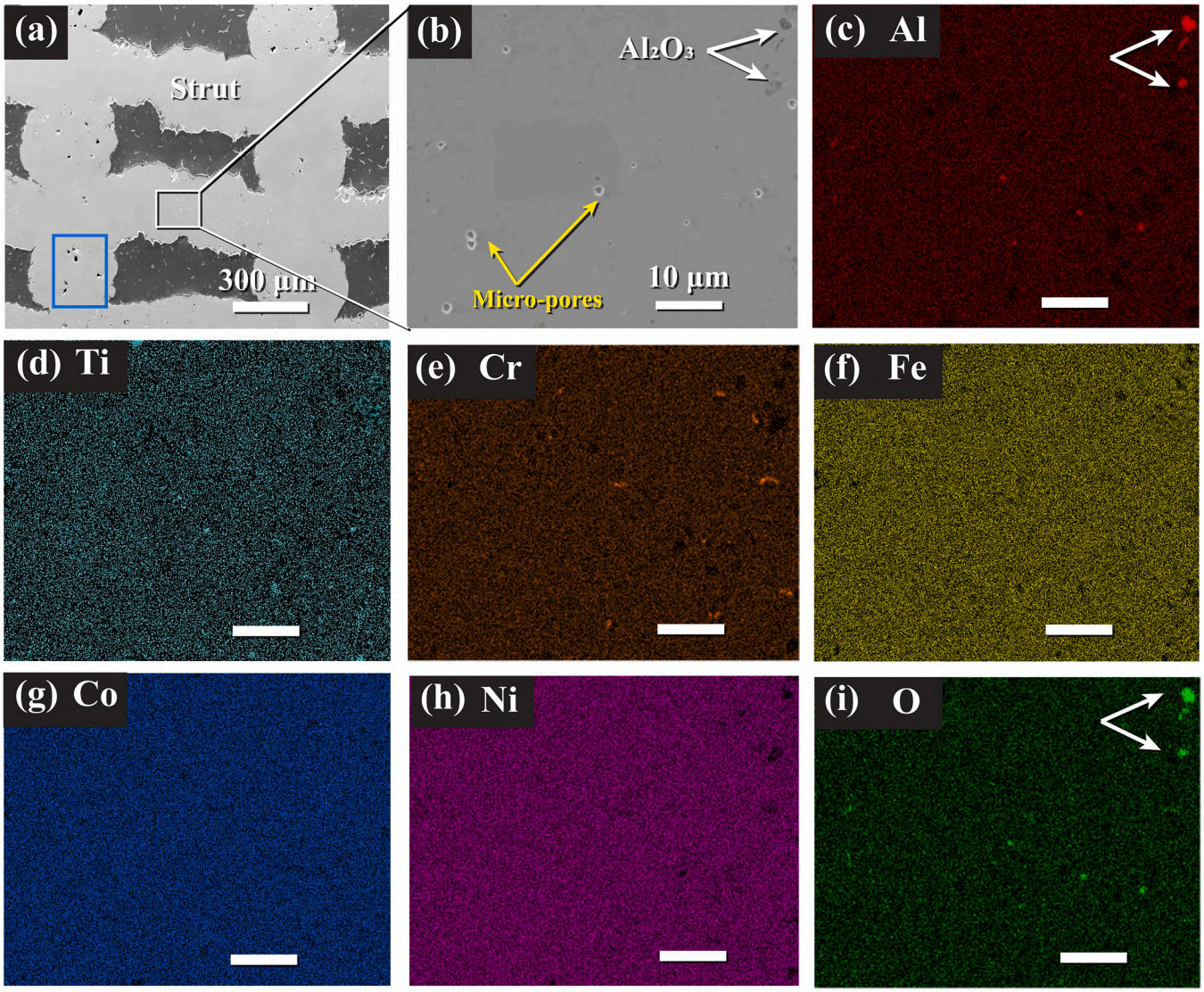

Fig. 3. Cross-sections of a microlattice after sintering at 1220 °C for 20 h and subsequent aging at 850 °C for 50 h. (a) SE micrograph at low magnification showing struts and channels (black epoxy). (b) Higher-magnification view of a strut showing micropores and Al_2O_3 particles (c-i) EDS maps of elemental distributions of the magnified view (b), scale bar: 10 μm.

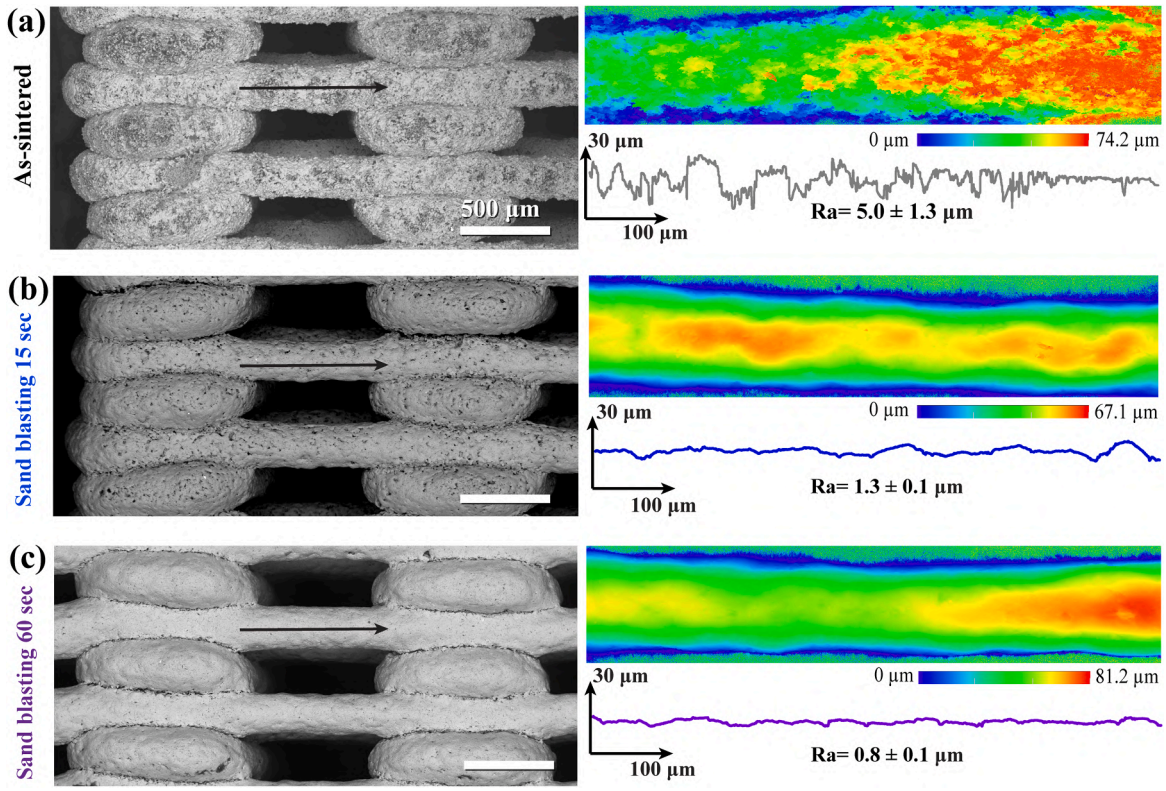

Fig. 4. Effect of sandblasting on surface quality of a sintered microlattice. (left column) SE micrographs of the side surface of lattices (a) before sandblasting, (b) after 15 s sandblasting and (c) after 60 s sandblasting; (right column) corresponding roughness profiles (waviness component subtracted) measured on the struts (along black arrows) at the side of the microlattice.

prevent premature failure during mechanical loading [78]. In the densest region of struts (white box, Fig. 3a), only micropores with sizes of ~1–3 µm are present, (yellow arrows, Fig. 3b). Occasional larger pores with 10–15 µm sizes are visible in the less dense regions (blue box, Fig. 3a). These large pores were most probably induced by heterogeneous powders packing and a locally lower packing of powders, and they are difficult to sinter [79]. Atomic interdiffusion during solid-state sintering is extensive, and it leads to both densification and homogenization, as seen from the uniform distribution of the six elements after sintering (EDS maps, Fig. 3c–h and Supplementary Fig. S6b–g). Although the specimens were protected by flowing ultra-high purity Ar during the entire sintering process, several Al_2O_3 particles (white arrows in Fig. 3b, c, i) are observed, reflecting the high affinity of Al to oxygen at high temperatures, despite using $TiAl_3$ precursor powders rather than elemental Al. The oxide pre-existing on $TiAl_3$ powder surfaces may also have coarsened into these particles.

As shown in Table 1, the compositions of the two alloys differ somewhat from the original, nominal composition ($Al_{10}Co_{25}Cr_8Fe_{15}Ni_{36}Ti_6$). Besides its lower Ti content, the low-Ti alloy ($Al_9Co_{26}Cr_7Fe_{16}Ni_{38}Ti_4$) is also slightly poorer in Al and Cr, and conversely a bit richer in Co, Fe, and Ni (but these differences are mostly within the error bars of the composition measurements). The high-Ti alloy ($Al_8Co_{25}Cr_7Fe_{15}Ni_{36}Ti_9$) is also somewhat poorer in Al and Cr, while Co, Fe, and Ni are at nominal values.

3.2. Surface treatment

Materials processed by beam-based powder fusion have poor surface finish with high roughness due to contamination, porosities, and unmelted particles; for instance, laser-printed Ti-6Al-4 V was reported to have a roughness average, Ra ≈ 17 µm [68],80–82]. By comparison, for our as-sintered HESA, struts on the side of the microlattices have a diameter of 247±13 µm, and a roughness Ra = 5.0±1.3 µm, as shown in Fig. 4a. Given the intricate architecture of the microlattices and many other printed objects, it is challenging to apply subtractive machining methods, such as milling and grinding, to improve surface finish. Here, we select sandblasting to remove contamination/oxidation from, and smoothen the surface of, the struts. After 15 sec blasting, the strut surface roughness decreases to Ra=1.3±0.1 µm; the surface has visibly changed color (from grey to metallic), with a few surface pores (black spots) shown in Fig. 4b. After sandblasting for 60 sec, the strut surface is much smoother, with a lower roughness of 0.8±0.1 µm (Fig. 4c). In addition to the straight struts in this microlattice, sandblasting also smoothens the surface of curved struts in a sintered gyroid cube and turbine blade, as shown in Supplementary Fig. S2. It is important to improve the surface finish of additively manufactured objects by either mechanical or chemical treatments during post-processing [81,83], as reducing surface roughness can effectively improve fatigue performance [81,84,85] as well as wear and corrosion resistance [86]. The surface waviness (Rc, mean height of profile elements) induced by the layer-by-layer deposition was measured as Rc=60.9±16.3 µm shown in Supplementary Fig. S3. This waviness could be reduced by longer sandblasting time. As demonstrated here, sandblasting is a simple and fast method to improve the surface finish for sintered HESA objects with intricate structures. Future work will study the effect of sandblasting on the mechanical properties of HESA lattices, probing the effects of blasting pressure, particle sizes, and treatment time on static and fatigue mechanical properties, as well as surface properties (corrosion and oxidation resistance).

3.3. Effect of Ti concentration on microstructures

Phase evolution of the nominal $Al_{10}Co_{25}Cr_8Fe_{15}Ni_{36}Ti_6$ composition, was predicted upon cooling from the melt as a function of temperature, at thermal equilibrium condition by the CALPHAD approach (Thermo-Cal with database: TCHEA5_High entropy alloys_v5.1). As shown in

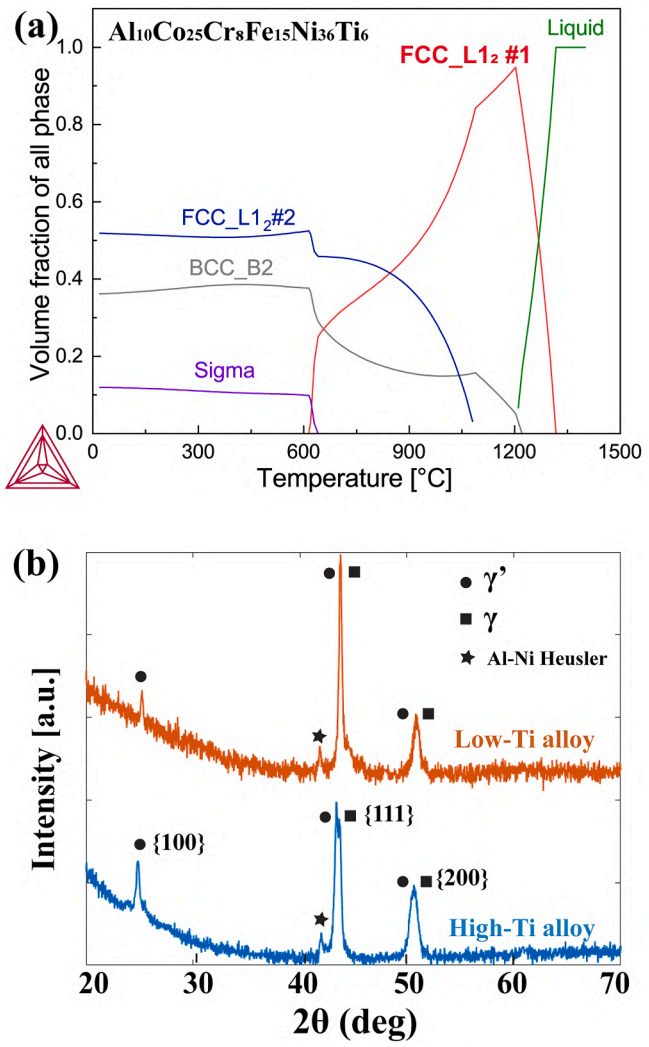

Fig. 5. (a) Phase evolution of $Al_{10}Co_{25}Cr_8Fe_{15}Ni_{36}Ti_6$ alloy as a function of temperature on solidification, as determined from CALPHAD-based calculations in Thermo-Cal software. (b) X-ray diffraction (XRD) patterns of low-Ti and high-Ti HESA lattices after homogenization and aging treatments, showing γ and γ' as the dominant phases, with small amounts of Heusler phase.

Fig. 5a, for an alloy undergoing solidification, the ordered FCC-$L1_2$ (#1) phase first forms (liquidus: 1317 °C; solidus: 1221 °C), and it is then predicted to transform into a mixture of γ' (FCC-$L1_2$ #2) and BCC-B2 ordered phases as temperature drops from 1221 to 640 °C. The specimens were annealed at 1220 °C, very close to the predicted solidus temperature of FCC-$L1_2$ (#1) phase, to homogenize all elements. Nevertheless, no evidence of liquid phase forming during sintering was observed in our samples. Between 640 °C and ambient temperature, the brittle sigma phase is also predicted to form, consuming the last of the FCC-$L1_2$ (#1) phase [87]. In disagreement with these predictions, the XRD patterns (Fig. 5b) of microlattices with low-Ti and high-Ti compositions, after homogenization (1220 °C for 20 h) and aging (850 °C for 50 h), exhibit FCC-γ and L12-γ' as the dominant phases, as in Ni-based [88,89] and Co-based superalloys [90], with small quantities of the Al-Ni-Co-rich Heusler phase [91] shown in Supplementary Fig. S4. Our observations are consistent with experimental results for $Al_{10}Co_{25}Cr_8Fe_{15}Ni_{36}Ti_6$ solidified *via* the Bridgeman method after similar heat treatments, as reported in Refs. [20,92].

When comparing the low-Ti and high-Ti alloys (Table 1), it is apparent that Ti concentration strongly affects the γ' precipitates, as illustrated in Fig. 6. In shallow-etched micrographs (Fig. 6a and c), the high-Ti alloy exhibits larger γ' precipitates with sharper-edged shapes, as compared to the low-Ti alloy. This morphology change in the high-Ti alloy implies a higher level of elastic anisotropy in the γ' precipitates which is also expected to influence mechanical properties [89]. Furthermore, the γ' volume fraction increases from 51 to 78 % as the Ti concentration increases from 4 to 9 at%, as measured in several different areas of deep-etched cross-sections (Fig. 6b and d). The 51 % γ' volume fraction for the low-Ti alloy is comparable to that reported by Daoud et al. [20] on a cast alloy of the same composition, $Al_{10}Co_{25}Cr_8Fe_{15}Ni_{36}Ti_6$, with the same homogenization treatment (1220 °C/20 h) and similar aging treatment (900 °C/50 h vs. our 850 °C/50 h). In our alloys, γ' precipitates are also observed at grain boundaries (yellow stripe, Fig. 6a) after aging; this implies that the γ' phase has high stability, as otherwise other phases might have formed at grain boundaries. EDS line scans across γ' precipitates within the γ matrix exhibit a similar profile in both alloys (Fig. 7): Ni, Ti, and Al are enriched in the ordered γ' phase, while Co, Fe, and Cr are enriched in the disordered γ matrix. Elemental distribution and corresponding partitioning ratios in the γ' and γ phases of both alloys are listed in Table 2: in particular, the Ti partitioning in the γ' phase is sharper in the Ti-rich alloy. Elemental concentrations for both phases were obtained by averaging the results from EDS line scans on four different regions in each sample. Moreover, the higher Ti concentrations in both phases (as compared to the Ti-poor alloy) also indicate an enhanced solid solution strengthening effect in both phases, in addition to the precipitation strengthening enhancement from larger γ' volume fraction. Nevertheless, all partitioning ratios are quite close to unity, indicating that the two phases have relatively close compositions; this implies a narrow γ+γ' two-phase region in these HESAs.

The lattice misfit (δ) in superalloys is defined as the difference in lattice constants a between the γ (FCC) and γ' ($L1_2$ structure) phases, divided by their mean value [93]:

$$\delta = \frac{(a_{\gamma'} - a_{\gamma})}{(a_{\gamma'} + a_{\gamma})/2} \tag{1}$$

By fitting the XRD patterns with two Pseudo-Voigt functions and a sum of baseline[95], the peak positions (2θ) of the {111} reflection, having the highest intensity, are determined for γ (green curve) and γ' (red curve) phases respectively, as shown in Fig. 8. The lattice constants (a_{γ} and $a_{\gamma'}$) for both phases are calculated using Bragg's law for cubic symmetry:

$$a = \frac{\lambda\sqrt{h^2 + k^2 + l^2}}{2\ sin\theta} \tag{2}$$

where λ is the X-ray wavelength (Cu $K_{\alpha 1}$, λ=1.542 Å), h, k, and l are the Miller indices of the investigated lattice plane. The calculated values of lattice constants and the misfits between γ/γ' phases in both low-Ti and high-Ti compositions are listed in Table 3. As shown in Fig. 8, the misfit increases from 0.23 to 0.63 % observed as a larger separation between {111} reflection of γ (green curve) and γ' (red curve) phases when the Ti concentration increases from 4 to 9 at%. Bramfitt's two-dimensional lattice mismatch theory [95] is also used to calculate the misfit (δ_B) between γ' precipitate and γ matrix as a comparison. Since both phases share a similar crystalline structure with cubic symmetry, Bramfitt's misfit equation is simplified for {111} reflection:

$$\delta_{B}^{(111)_{\gamma}} = \frac{d_{[110]_{\gamma'}} - d_{[110]_{\gamma}}}{d_{[110]_{\gamma'}}} = \frac{\sqrt{2}/2a_{\gamma'} - \sqrt{2}/2a_{\gamma}}{\sqrt{2}/2a_{\gamma'}} \tag{3}$$

where $d_{[110]_{\gamma'}}$ and $d_{[110]_{\gamma}}$ are the interatomic spacing along [110] direction for the γ' and γ phases. The calculated δ_B is quite similar to the δ listed in Table 3 as well. A larger misfit helps inhibit dislocation glide through coherent interface boundaries between the γ' and γ phases, thus increasing strength [92,96]. Positive misfits are also observed in some Ni-based superalloys such as CMSX-4 [93], most Co-based superalloys [94], and a Ni-Co-Fe-based HESA ($Ni_{48}Co_{17}Fe_9Al_{10}Cr_7Ti_6Mo_1Nb_1W_{0.4}C_{0.4}$) [4].

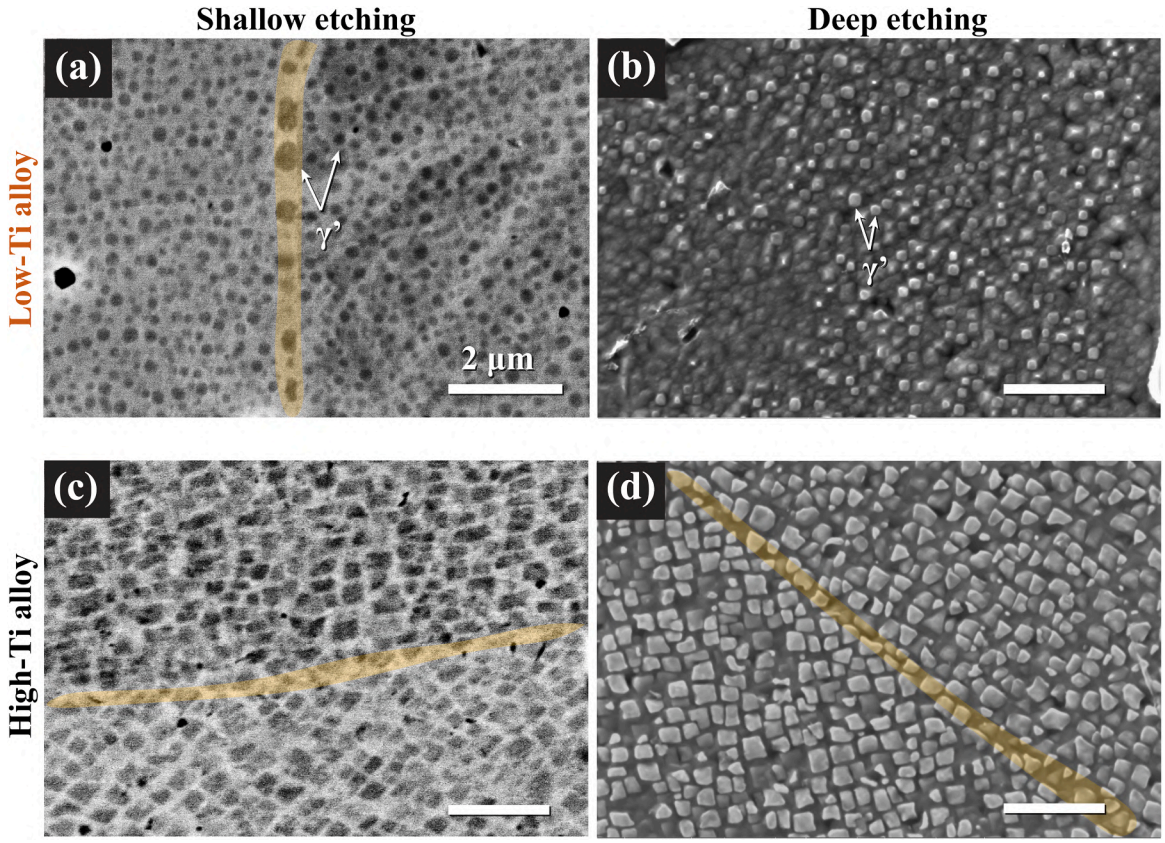

Fig. 6. SE micrographs of γ/γ' microstructures of (a-b) low-Ti alloy and (c-d) high-Tialloy after (left column) shallow etching and (right column) deep etching. Grain boundaries are highlighted with a yellow band.

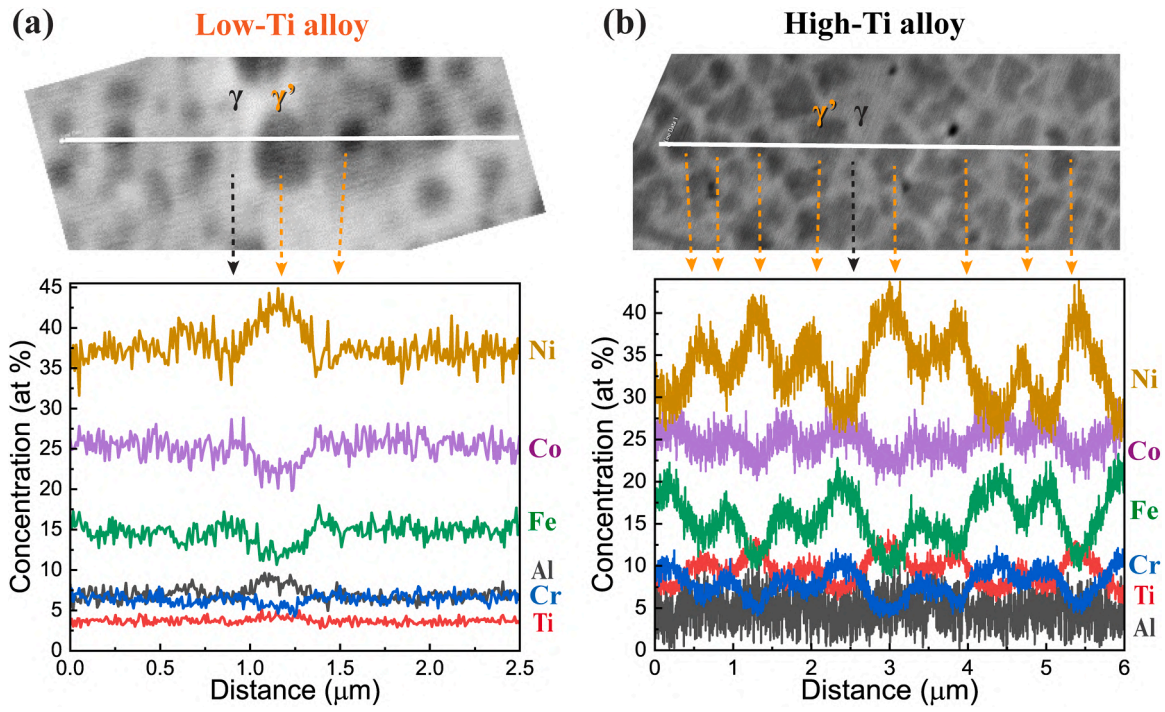

Fig. 7. Upper row: SE images of EDS line scan across γ' precipitates and γ matrix in microlattices with low-Ti and high-Ti compositions; Bottom row: corresponding elemental concentrations curves for each EDS measurement. The γ and γ' phases on scanned lines and their elemental concentrations are correlated by dashed arrows.

Table 2
Elemental concentrations c (at%) and partitioning ratios (-) between the γ' and γ phases for the low-Ti and high-Ti compositions. Estimated error on composition is 1.5 at% (calculated from the standard deviation of multiple EDS measurements).

		Al	Co	Cr	Fe	Ni	Ti
Low-Ti alloy	c_γ	6.9	25.5	6.5	14.8	36.9	3.8
	$c_{\gamma'}$	8.2	22.9	5.7	12.8	41.1	4.1
	$c_{\gamma'}/c_\gamma$	1.2	0.90	0.88	0.86	1.1	1.1
High-Ti alloy	c_γ	5.4	26.1	9.2	17.9	30.1	8.0
	$c_{\gamma'}$	7.2	22.4	5.3	11.3	39.0	11.7
	$c_{\gamma'}/c_\gamma$	1.3	0.86	0.58	0.63	1.3	1.5

Table 3
Peak positions (2θ) of the {111} reflection, lattice constants of γ and γ' phases and calculated misfits (δ and δ_B) between two phases for the low-Ti and high-Ti compositions.

Composition	Phase	2θ (°)	Lattice constant *a* (Å)	δ (%)	δ_B (%)
Low-Ti alloy $Al_9Co_{26}Cr_7Fe_{16}Ni_{38}Ti_4$	γ	43.93	3.57	0.23	0.23
	γ'	43.82	3.58		
High-Ti alloy $Al_8Co_{25}Cr_7Fe_{15}Ni_{36}Ti_9$	γ	43.70	3.59	0.63	0.63
	γ'	43.41	3.61		

In high- and medium-entropy superalloys, refractory elements such as Hf, W, Mo, and Zr have been added to promote the γ' phase formation, increase lattice misfits, and enhance high-temperature properties [21,97]. However, refractory element addition in the $Al_{10}Co_{25}Cr_8Fe_{15}Ni_{36}Ti_6$ alloy may increase the amount of needle-shaped Heusler phase [98], whose brittleness can reduce ductility and creep resistance [21,99]. Conversely, Ti additions used here increase the size, volume fraction, and lattice constant of the strengthening γ' precipitates effectively, without introducing detrimental phases and adding costly refractory elements.

3.4. Mechanical properties of HESA microlattices

3.4.1. Ambient temperature

Fig. 9a shows compressive stress-strain curves for the low-Ti and high-Ti lattices; the Ti addition has a marked effect on strength, with a 2.5-fold increase in yield strength, from 53±3 to 127±6 MPa respectively. The Vickers microhardness of struts also increases with Ti concentration, by a factor ~1.25, as shown in Fig. 9b. Increasing Ti concentration not only increases the γ' volume fraction, it also contributes to solid-solution strengthening in both precipitates and matrix, as measured by higher Ti concentrations in both phases (especially in the γ' precipitates) in the high-Ti alloy (Fig. 7b and Table 2). The stress-strain curves reveal that both lattices are ductile and deform steadily until 60 % compressive strain, without catastrophic failures. Serrations on the stress-strain curves (orange arrows) of the low-Ti lattice are visible in Fig. 9a: they are attributed to cracking of struts at stress concentrations, inducing plastic instability during compression, as confirmed by observation of deformed lattices (Supplementary Fig. S5). According to a previous finite-elements modeling (FEM) study of compressive deformation on an orthogonal lattice with identical geometry, stress, and strain are concentrated at notches between the upper and lower struts of two consecutive layers [48,68]. A tensile strain is predicted to exist on the horizontal struts, induced by lateral expansion of the lattice, observed as the notable expansion of microlattices along the horizontal direction after compression (Supplementary Fig. S5a and c). Also observed here on a cross-section of the deformed microlattice with the high-Ti composition shown in Fig. 10a, the resulting tensile stress concentration leads to the opening of cracks (black arrow) in the region close to notches. The horizontal strust is then bent away from its original position (dashed white lines) under shear deformation (Fig. 10a). A magnified view at a plastic hinge, in a region with high local bending strain, displays a shear zone in which the γ' precipitates are heavily deformed from their original cuboidal shape by shearing, as shown in Fig. 10b. In the shear zone, the γ' precipitates elongated along the shear direction have an average aspect ratio of 2.65 ±0.50, much higher than the γ' precipitates (aspect ratio of 1.23±0.14) outside the shear zone, according to ImageJ calculation. This result indicates severe plastic deformation at the plastic hinge with high local shear (tensile/compressive) ductility able to accommodate large plastic strains.

3.4.2. Elevated temperatures

Given their higher strength and better ductility at ambient temperature, the high-Ti lattices were further tested in uniaxial compression at elevated temperatures, between 700 and 1000 °C. They were deformed at a strain rate of 1.2×10^{-3} s^{-1} up to 60 % strain, as illustrated in Fig. 11a. As expected, the lattice strength decreases with increasing temperatures, while their compressive ductility remains high, without large stress drops on the stress-strain curve which would be indicative of extensive strut fracture. The specific strengths are plotted in Fig. 11b as a function of the temperature for representative bulk HEAs without refractory elements; it is calculated as the ultimate strength (measured during compressive or tensile testing) divided by the density [20,

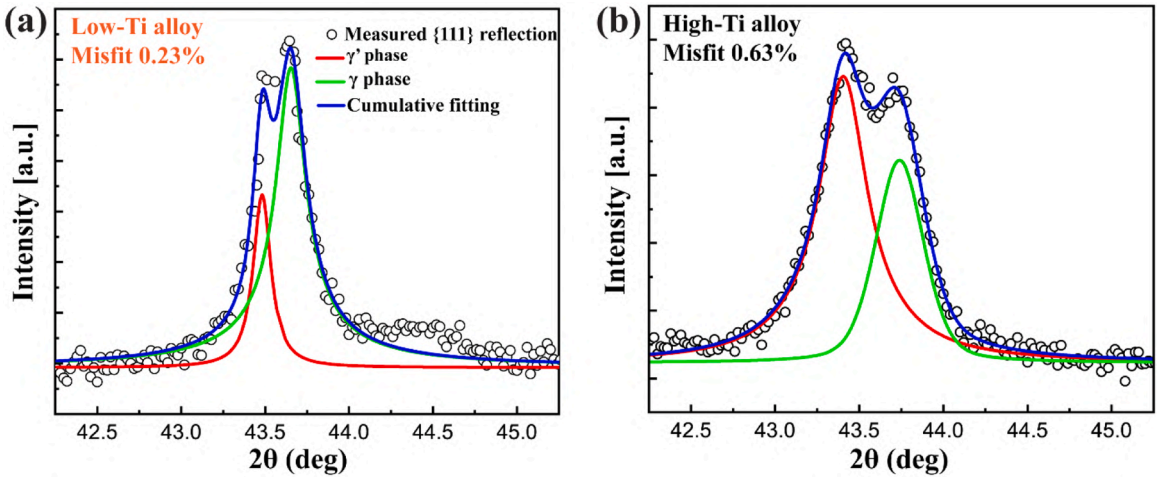

Fig. 8. Peak fittings and deconvolution of the {111} XRD reflection for the γ' and γ phases in (a) low-Ti and (b) high-Ti alloys.

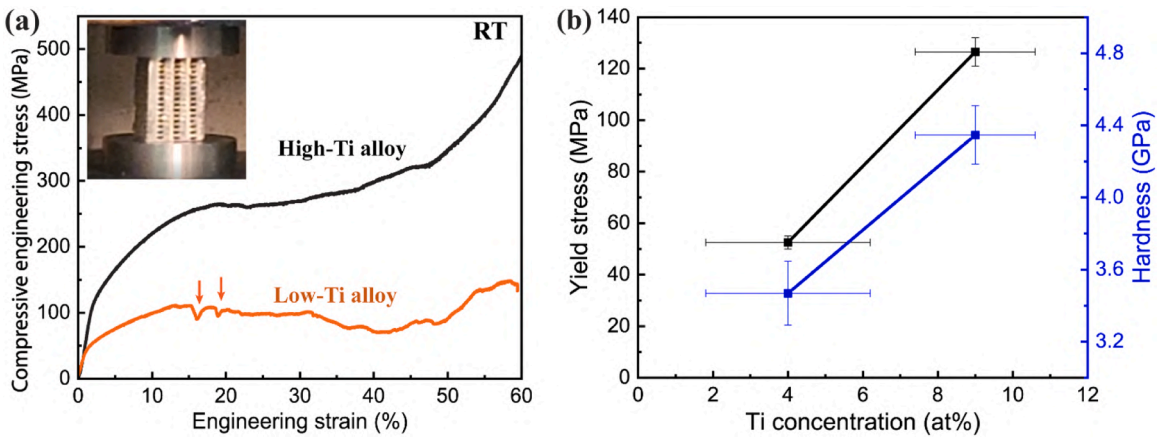

Fig. 9. (a) Compressive engineering stress-strain curves of microlattices with low- and high-Ti compositions at ambient temperature. (b) Yield stress of lattices and Vickers microhardness of struts for both compositions.

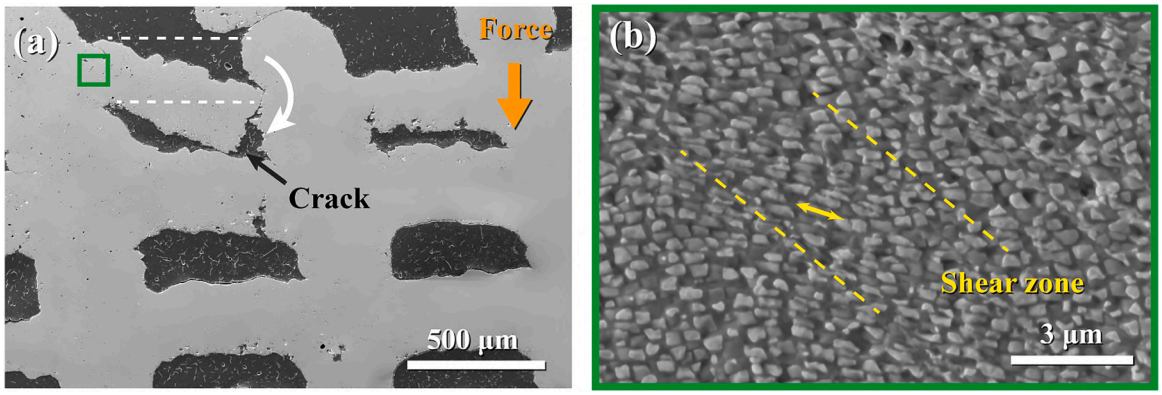

Fig. 10. (a) SEM micrograph of a cross-section of a high-Ti HESA microlattice after compressive deformation to 61 % strain at ambient temperature. (b) A magnified view of the green box marked in (a), at a region with a large bending strain, with a yellow arrow showing sheared γ' precipitates within a shear zone in the heavily deformed plastic hinge region.

100–104]; for our lattice samples, the stress at 20 % strain is used. The relative density, denoted as ρ/ρ_s, of our sintered HESA lattices falls between 30 and 42 %, with ρ_s=7.37 g/cm^3 representing the bulk density calculated from elemental density. It is apparent from Fig. 11b that our lattices exhibit a higher specific strength as compared to bulk Inconel 617 and other HEAs over a wide range of temperatures, and a somewhat lower specific strength than bulk $Al_{10}Co_{25}Cr_8Fe_{15}Ni_{36}Ti_6$, except at 1000 °C. Lattices are inherently weaker, even after density compensation, than the corresponding bulk alloy [105]. However, in the bulk, our high-Ti composition ($Al_8Co_{25}Cr_7Fe_{15}Ni_{36}Ti_9$) is expected to be stronger than the literature $Al_{10}Co_{25}Cr_8Fe_{15}Ni_{36}Ti_6$ HESA [20], due to a higher γ' phase fraction (78 vs. 46 %)[20]. Also, the strengthening effect of the harder γ' phase is more notable at high temperatures. Thus, it is apparent that the overall mechanical properties of HESA lattices can be further enhanced, particularly at high temperatures, by optimal alloying additions (such as Ti studied here) and by eliminating defects leading to stress concentrations.

4. Conclusions

Inks containing a blend of six metallic powders (Cr, Ti, Fe, Ni, Co, and $TiAl_3$) were 3D-extruded to print high-entropy superalloys with low-Ti ($Al_9Co_{26}Cr_7Fe_{16}Ni_{38}Ti_4$) and high-Ti ($Al_8Co_{25}Cr_7Fe_{15}Ni_{36}Ti_9$) compositions. Five main conclusions can be drawn:

(1) Printed green bodies were first heated up to 400 °C to remove solvent and binder, sintered at 1220 °C to densify struts and homogenize elements by interdiffusion, and finally aged at 850 °C to achieve a γ/γ' microstructures.
(2) Miniature objects with intricate architectures were created with a high uniform shrinkage, but without cracks or warpage: 0–90° lattices (for sandwich structures), turbine blades (with hollow lattice core), double-walled gyroid cubes (for heat exchangers), and turbo compressor wheels.
(3) By increasing Ti concentrations from 4 to 9 at%, the γ' precipitates increase in volume fraction from 51 to 78 %, and their shape evolves to sharper-edged cube with larger elastic anisotropy.
(4) Titanium additions increase the strength of the microlattices at ambient temperature, while maintaining high compressive ductility (achieving 60% strain without catastrophic failure). The HESA microlattices display a low density, between 2.29 and 3.15 g/cm^3, but with high specific strength as compared to other HEAs, especially at high temperatures.
(5) Sandblasting of sintered objects for a short time removes surface oxidation and smooths the surface of struts effectively. The surface roughness (Ra) of struts decreases from 5.0±1.3 μm in the as-sintered state to 0.8±0.1 μm after blasting for 60 sec.

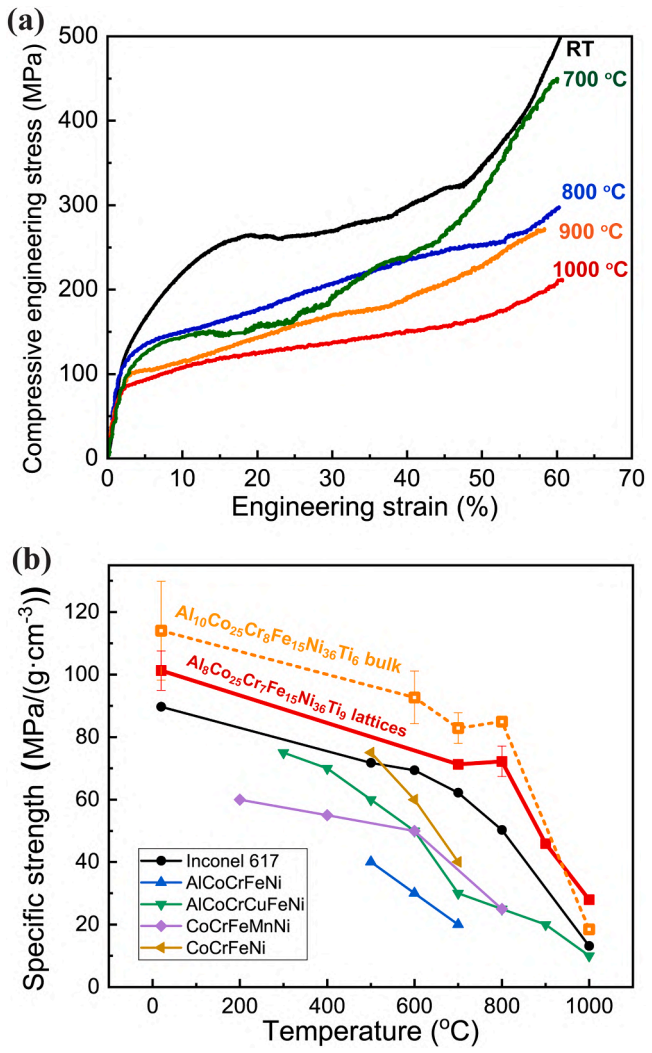

Fig. 11. (a) Compressive engineering stress-strain curves of high-Ti HESA microlattices at various temperatures. (b) Comparison of the specific strength of present high-Ti $Al_8Co_{25}Cr_7Fe_{15}Ni_{36}Ti_9$ HESA microlattices (compressive), with tensile or compressive specific strength of bulk $Al_{10}Co_{25}Cr_8Fe_{15}Ni_{36}Ti_6$ [20], bulk Ti-free HESA (equiatomic AlCoCrFeNi [101], CoCrFeMnNi [102], CoCrFeNi [103], and AlCrCuNiFeCo [104]), and bulk Inconel 617 superalloy [100].

CRediT authorship contribution statement

Ming Chen: Conceptualization, Data curation, Formal analysis, Investigation, Methodology, Resources, Writing – original draft, Writing – review & editing. **Dingchang Zhang:** Methodology, Writing – review & editing, Software. **Ya-Chu Hsu:** Methodology, Writing – review & editing. **David C. Dunand:** Conceptualization, Funding acquisition, Project administration, Resources, Supervision, Writing – review & editing.

Declaration of competing interest

The authors declare the following financial interests/personal relationships which may be considered as potential competing interests:

DCD discloses a financial interest in Metalprinting, Inc. (South Korea) which is active in ink-based materials printing.

Data availability

The data that support the findings of the present study are available from the corresponding author upon reasonable request.

Acknowledgments

This research received financial support from the National Science Foundation (NSF DMR-2004769). The work made use of the J.B. Cohen X-Ray Diffraction Facility supported by the MRSEC program *via* the National Science Foundation (DMR-2308691) at the Materials Research Center of Northwestern University and the Soft and Hybrid Nanotechnology Experimental (SHyNE) Resource (NSF ECCS-1542205). This work also made use of the EPIC facility of Northwestern University's NUANCE Center, which has received support from the Soft and Hybrid Nanotechnology Experimental (SHyNE) Resource (NSF ECCS-1542205); the MRSEC program (NSF DMR-1720139) at the Materials Research Center; the International Institute for Nanotechnology (IIN); the Keck Foundation; and the State of Illinois, through the IIN. We thank Prof. Samuel Stupp (Northwestern University) for the use of his Bioplotter 3D printer for direct ink writing process.

Supplementary materials

Supplementary material associated with this article can be found, in the online version, at doi:10.1016/j.actamat.2024.120055.

References

[1] J.-W. Yeh, S.-K. Chen, S.-J. Lin, J.-Y. Gan, T.-S. Chin, T.-T. Shun, C.-H. Tsau, S.-Y. Chang, Nanostructured high-entropy alloys with multiple principal elements: novel alloy design concepts and outcomes, Adv. Eng. Mater. 6 (2004) 299–303, https://doi.org/10.1002/adem.200300567.

[2] B. Cantor, I.T.H. Chang, P. Knight, A.J.B. Vincent, Microstructural development in equiatomic multicomponent alloys, Mater. Sci. Eng. A 375–377 (2004) 213–218, https://doi.org/10.1016/j.msea.2003.10.257.

[3] S. Praveen, H.S. Kim, High-entropy alloys: potential candidates for high-temperature applications – an overview, Adv. Eng. Mater. 20 (2018) 1–22.

[4] T.K. Tsao, A.C. Yeh, C.M. Kuo, K. Kakehi, H. Murakami, J.W. Yeh, S.R. Jian, The high temperature tensile and creep behaviors of high entropy superalloy, Sci. Rep. 7 (2017), https://doi.org/10.1038/s41598-017-13026-7.

[5] J. Chen, X. Zhou, W. Wang, B. Liu, Y. Lv, W. Yang, D. Xu, Y. Liu, A review on fundamental of high entropy alloys with promising high–temperature properties, J. Alloy. Compd. 760 (2018) 15–30, https://doi.org/10.1016/j.jallcom.2018.05.067.

[6] B. Cantor, I.T.H. Chang, P. Knight, A.J.B. Vincent, Microstructural development in equiatomic multicomponent alloys, Mater. Sci. Eng. A 375–377 (2004) 213–218, https://doi.org/10.1016/j.msea.2003.10.257.

[7] D.G. Shaysultanov, N.D. Stepanov, G.A. Salishchev, M.A. Tikhonovsky, Effect of heat treatment on the structure and hardness of high-entropy alloys CoCrFeNiMnV x (x= 0.25, 0.5, 0.75, 1), Phys. Metal. Metallogr. 118 (2017) 579–590.

[8] Z.G. Zhu, K.H. Ma, X. Yang, C.H. Shek, Annealing effect on the phase stability and mechanical properties of (FeNiCrMn)(100−x) Cox high entropy alloys, J. Alloy. Compd. 695 (2017) 2945–2950.

[9] Y. Zhang, T.T. Zuo, Z. Tang, M.C. Gao, K.A. Dahmen, P.K. Liaw, Z.P. Lu, Microstructures and properties of high-entropy alloys, Prog. Mater. Sci. 61 (2014) 1–93, https://doi.org/10.1016/j.pmatsci.2013.10.001.

[10] W.R. Wang, W.L. Wang, S.C. Wang, Y.C. Tsai, C.H. Lai, J.W. Yeh, Effects of Al addition on the microstructure and mechanical property of Al_xCoCrFeNi high-entropy alloys, Intermetall. (Bark.) 26 (2012) 44–51, https://doi.org/10.1016/J.INTERMET.2012.03.005.

[11] H.M. Daoud, A. Manzoni, R. Völkl, N. Wanderka, U. Glatzel, Microstructure and tensile behavior of $Al_8Co_{17}Cr_{17}Cu_8Fe_{17}Ni_{33}$ (at.%) high-entropy alloy, JOM 65 (2013) 1805–1814, https://doi.org/10.1007/s11837-013-0756-3.

[12] Y. Lu, K. Zhang, B. Zhao, X. Dong, F. Sun, B. Zhou, Y. Zhen, L. Zhang, Balanced mechanical properties of $Al_{0.3}$CoCrFeNiTi$_x$ high-entropy alloys by tailoring Ti content and heat treatment, Mater. Sci. Eng.: A 866 (2023) 144677.

[13] J. Shen, A.C. Martin, N. Schell, C. Fink, J.P. Oliveira, Microstructures in arc-welded $Al_{10}Co_{25}Cr_8Fe_{15}Ni_{36}Ti_6$ and $Al_{10.87}Co_{21.74}Cr_{21.74}Cu_{2.17}Fe_{21.74}Ni_{21.74}$ multi-principal element alloys: Comparison between experimental data and thermodynamic predictions, Mater. Today Commun. 34 (2023) 104784.

[14] B. Gwalani, V. Soni, D. Choudhuri, M. Lee, J.Y. Hwang, S.J. Nam, H. Ryu, S. H. Hong, R. Banerjee, Stability of ordered L_{12} and B_2 precipitates in face centered cubic based high entropy alloys - $Al_{0.3}$CoFeCrNi and $Al_{0.3}$CuFeCrNi$_2$, Scr. Mater. 123 (2016) 130–134, https://doi.org/10.1016/J.SCRIPTAMAT.2016.06.019.

[15] I.S. Wani, T. Bhattacharjee, S. Sheikh, I.T. Clark, M.H. Park, T. Okawa, S. Guo, P. P. Bhattacharjee, N. Tsuji, Cold-rolling and recrystallization textures of a nano-lamellar AlCoCrFeNi$_{2.1}$ eutectic high entropy alloy, Intermetall. (Bark.) 84 (2017) 42–51, https://doi.org/10.1016/J.INTERMET.2016.12.018.

[16] I.S. Wani, T. Bhattacharjee, S. Sheikh, Y.P. Lud, S. Chatterjee, P.P. Bhattacharjeea, S. Guo, N. Tsujib, Ultrafine-grained AlCoCrFeNi$_{2.1}$ eutectic high-entropy alloy, Mater. Res. Lett. 4 (2016) 174–179, https://doi.org/10.1080/21663831.2016.1160451.

[17] Y.T. Chen, Y.J. Chang, H. Murakami, S. Gorsse, A.C. Yeh, Designing high entropy superalloys for elevated temperature application, Scr. Mater. 187 (2020) 177–182, https://doi.org/10.1016/j.scriptamat.2020.06.002.

[18] J.W. Yeh, Physical metallurgy of high-entropy alloys, JOM 67 (2015) 2254–2261, https://doi.org/10.1007/s11837-015-1583-5.

[19] C. Kenel, N.R. Geisendorfer, R.N. Shah, D.C. Dunand, Hierarchically-porous metallic scaffolds via 3D extrusion and reduction of oxide particle inks with salt space-holders, Addit. Manuf. 37 (2021) 101637, https://doi.org/10.1016/j.addma.2020.101637.

[20] H.M. Daoud, A.M. Manzoni, N. Wanderka, U. Glatzel, High-Temperature Tensile Strength of Al10Co25Cr8Fe15Ni36Ti6 Compositionally Complex Alloy (High-Entropy Alloy), JOM 67 (2015) 2271–2277, https://doi.org/10.1007/s11837-015-1484-7.

[21] S. Haas, A.M. Manzoni, M. Holzinger, U. Glatzel, Influence of high melting elements on microstructure, tensile strength and creep resistance of the compositionally complex alloy $Al_{10}Co_{25}Cr_8Fe_{15}Ni_{36}Ti_6$, Mater. Chem. Phys. 274 (2021) 125163, https://doi.org/10.1016/j.matchemphys.2021.125163.

[22] M.M. Attallah, R. Jennings, X. Wang, L.N. Carter, Additive manufacturing of Ni-based superalloys: the outstanding issues, MRS Bull 41 (2016) 758–764, https://doi.org/10.1557/mrs.2016.211.

[23] S.P. Murray, K.M. Pusch, A.T. Polonsky, C.J. Torbet, G.G.E. Seward, N. Zhou, S.A. J. Forsik, P. Nandwana, M.M. Kirka, R.R. Dehoff, W.E. Slye, T.M. Pollock, A defect-resistant Co–Ni superalloy for 3D printing, Nat. Commun. 11 (2020), https://doi.org/10.1038/s41467-020-18775-0.

[24] C. Haase, F. Tang, M.B. Wilms, A. Weisheit, B. Hallstedt, Combining thermodynamic modeling and 3D printing of elemental powder blends for high-throughput investigation of high-entropy alloys – towards rapid alloy screening and design, Mater. Sci. Eng.: A 688 (2017) 180–189, https://doi.org/10.1016/j.msea.2017.01.099.

[25] B. Gwalani, S. Gangireddy, S. Shukla, C.J. Yannetta, S.G. Valentin, R.S. Mishra, R. Banerjee, Compositionally graded high entropy alloy with a strong front and ductile back, Mater. Today Commun. 20 (2019), https://doi.org/10.1016/j.mtcomm.2019.100602.

[26] T. Borkar, V. Chaudhary, B. Gwalani, D. Choudhuri, C.V. Mikler, V. Soni, T. Alam, R.V. Ramanujan, R. Banerjee, A combinatorial approach for assessing the magnetic properties of high entropy alloys: role of Cr in $AlCo_xCr_{1-x}FeNi$, Adv. Eng. Mater. 19 (2017), https://doi.org/10.1002/adem.201700048.

[27] M.A. Melia, S.R. Whetten, R. Puckett, M. Jones, M.J. Heiden, N. Argibay, A. B. Kustas, High-throughput additive manufacturing and characterization of refractory high entropy alloys, Appl. Mater. Today 19 (2020), https://doi.org/10.1016/j.apmt.2020.100560.

[28] H. Dobbelstein, M. Thiele, E.L. Gurevich, E.P. George, A. Ostendorf, Direct metal deposition of refractory high entropy alloy MoNbTaW, Phys. Proced. 83 (2016) 624–633, https://doi.org/10.1016/j.phpro.2016.08.065.

[29] H. Dobbelstein, E.L. Gurevich, E.P. George, A. Ostendorf, G. Laplanche, Laser metal deposition of a refractory TiZrNbHfTa high-entropy alloy, Addit. Manuf. 24 (2018) 386–390, https://doi.org/10.1016/j.addma.2018.10.008.

[30] C. Han, Q. Fang, Y. Shi, S.B. Tor, C.K. Chua, K. Zhou, Recent advances on high-entropy alloys for 3D printing, Adv. Mater. 32 (2020), https://doi.org/10.1002/adma.201903855.

[31] S. Hocine, H. Van Swygenhoven, S. Van Petegem, Verification of selective laser melting heat source models with operando X-ray diffraction data, Addit. Manuf. 37 (2021) 101747.

[32] M. Chen, M. Simonelli, S. Van Petegem, Y. Yau Tse, C. Sin Ting Chang, M. Grazyna Makowska, D. Ferreira Sanchez, H. Moens-Van Swygenhoven, A quantitative study of thermal cycling along the build direction of Ti-6Al-4V produced by laser powder bed fusion, Mater. Des. 225 (2023) 111458, https://doi.org/10.1016/j.matdes.2022.111458.

[33] N. Shen, K. Chou, Numerical Thermal Analysis in Electron Beam Additive Manufacturing with Preheating Effects, 2012.

[34] W.J. Sames, K.A. Unocic, R.R. Dehoff, T. Lolla, S.S. Babu, Thermal effects on microstructural heterogeneity of Inconel 718 materials fabricated by electron beam melting, J. Mater. Res. 29 (2014) 1920–1930, https://doi.org/10.1557/jmr.2014.140.

[35] A.A. Antonysamy, Microstructure, Texture and Mechanical Property Evolution During Additive Manufacturing of Ti6Al4V Alloy For Aerospace Applications, The University of Manchester (United Kingdom, 2012.

[36] N.A. Kistler, A.R. Nassar, E.W. Reutzel, D.J. Corbin, A.M. Beese, Effect of directed energy deposition processing parameters on laser deposited Inconel® 718: Microstructure, fusion zone morphology, and hardness, J. Laser Appl. 29 (2017), https://doi.org/10.2351/1.4979702.

[37] P.L. Blackwell, The mechanical and microstructural characteristics of laser-deposited IN718, J. Mater. Process. Technol. 170 (2005) 240–246, https://doi.org/10.1016/J.JMATPROTEC.2005.05.005.

[38] L.L. Parimi, G. Ravi, D. Clark, M.M. Attallah, Microstructural and texture development in direct laser fabricated IN718, Mater. Charact. 89 (2014) 102–111, https://doi.org/10.1016/J.MATCHAR.2013.12.012.

[39] H. Galarraga, R.J. Warren, D.A. Lados, R.R. Dehoff, M.M. Kirka, P. Nandwana, Effects of heat treatments on microstructure and properties of Ti-6Al-4V ELI alloy fabricated by electron beam melting (EBM), Mater. Sci. Eng.: A 685 (2017) 417–428, https://doi.org/10.1016/j.msea.2017.01.019.

[40] Y.-L. Hao, S.-J. Li, R. Yang, Biomedical titanium alloys and their additive manufacturing, Rare Metal. 35 (2016) 661–671, https://doi.org/10.1007/s12598-016-0793-5.

[41] D. Cormier, O. Harrysson, T. Mahale, H. West, Freeform Fabrication of Titanium Aluminide via Electron Beam Melting Using Prealloyed and Blended Powders, Research Letters in Materials Science 2007 (2007) 1–4, https://doi.org/10.1155/2007/34737.

[42] A. Amar, J. Li, S. Xiang, X. Liu, Y. Zhou, G. Le, X. Wang, F. Qu, S. Ma, W. Dong, Q. Li, Additive manufacturing of high-strength CrMnFeCoNi-based High Entropy Alloys with TiC addition, Intermetall. (Bark.) 109 (2019) 162–166, https://doi.org/10.1016/j.intermet.2019.04.005.

[43] E. Loria, Superalloys 718, 625, 706 and Various Derivatives, 1994, p. 1994. Pittsburgh.

[44] M.B. Henderson, D. Arrell, R. Larsson, M. Heobel, G. Marchant, Nickel based superalloy welding practices for industrial gas turbine applications, Sci. Technol. Weld. Join. 9 (2004) 13–21, https://doi.org/10.1179/136217104225017099.

[45] A.E. Jakus, S.L. Taylor, N.R. Geisendorfer, D.C. Dunand, R.N. Shah, Metallic architectures from 3D-printed powder-based liquid inks, Adv. Funct. Mater. 25 (2015) 6985–6995, https://doi.org/10.1002/adfm.201503921.

[46] A. De Luca, C. Kenel, S. Griffiths, S.S. Joglekar, C. Leinenbach, D.C. Dunand, Microstructure and defects in a Ni-Cr-Al-Ti γ/γ' model superalloy processed by laser powder bed fusion, Mater. Des. 201 (2021) 109531, https://doi.org/10.1016/J.MATDES.2021.109531.

[47] L.N. Carter, M.M. Attallah, R.C. Reed, Laser Powder Bed Fabrication of Nickel-Base Superalloys: Influence of Parameters; Characterisation, Quantification and Mitigation of Cracking, in: Superalloys 2012, Wiley, 2012, pp. 577–586, https://doi.org/10.1002/9781118516430.ch64.

[48] D. Zhang, C. Kenel, D.C. Dunand, Microstructure and properties of additively-manufactured WC-Co microlattices and WC-Cu composites, Acta Mater. 221 (2021) 117420, https://doi.org/10.1016/j.actamat.2021.117420.

[49] S.L. Taylor, R.N. Shah, D.C. Dunand, Ni-Mn-Ga micro-trusses via sintering of 3D-printed inks containing elemental powders, Acta Mater. 143 (2018) 20–29, https://doi.org/10.1016/j.actamat.2017.10.002.

[50] S.L. Taylor, A.E. Jakus, R.N. Shah, D.C. Dunand, Iron and nickel cellular structures by sintering of 3D-printed oxide or metallic particle inks, Adv. Eng. Mater. 19 (2017) 1600365, https://doi.org/10.1002/adem.201600365.

[51] S.L. Taylor, A.J. Ibeh, A.E. Jakus, R.N. Shah, D.C. Dunand, NiTi-Nb micro-trusses fabricated via extrusion-based 3D-printing of powders and transient-liquid-phase sintering, Acta Biomater. 76 (2018) 359–370, https://doi.org/10.1016/j.actbio.2018.06.015.

[52] X. Wang, Y. Sun, C. Peng, H. Luo, R. Wang, D. Zhang, Transitional suspensions containing thermosensitive dispersant for three-dimensional printing, ACS Appl. Mater. Interface. 7 (2015) 26131–26136, https://doi.org/10.1021/acsami.5b07913.

[53] S. Eqtesadi, A. Motealleh, F.H. Perera, P. Miranda, A. Pajares, R. Wendelbo, F. Guiberteau, A.L. Ortiz, Fabricating geometrically-complex B4C ceramic components by robocasting and pressureless spark plasma sintering, Scr. Mater. 145 (2018) 14–18, https://doi.org/10.1016/J.SCRIPTAMAT.2017.10.001.

[54] N. Kleger, M. Cihova, K. Masania, A.R. Studart, J.F. Löffler, 3D printing of salt as a template for magnesium with structured porosity, Adv. Mater. 31 (2019), https://doi.org/10.1002/adma.201903783.

[55] S. Mooraj, S.S. Welborn, S. Jiang, S. Peng, J. Fu, S. Baker, E.B. Duoss, C. Zhu, E. Detsi, W. Chen, Three-dimensional hierarchical nanoporous copper via direct ink writing and dealloying, Scr. Mater. 177 (2020) 146–150, https://doi.org/10.1016/J.SCRIPTAMAT.2019.10.013.

[56] B. Song, C. Kenel, D.C. Dunand, 3D ink-extrusion printing and sintering of Ti, Ti-TiB and Ti-TiC microlattices, Addit. Manuf. 35 (2020) 101412, https://doi.org/10.1016/J.ADDMA.2020.101412.

[57] S.L. Taylor, A.J. Ibeh, A.E. Jakus, R.N. Shah, D.C. Dunand, NiTi-Nb micro-trusses fabricated via extrusion-based 3D-printing of powders and transient-liquid-phase sintering, Acta Biomater. 76 (2018) 359–370, https://doi.org/10.1016/J.ACTBIO.2018.06.015.

[58] S.L. Taylor, R.N. Shah, D.C. Dunand, Microstructure and porosity evolution during sintering of Ni-Mn-Ga wires printed from inks containing elemental powders, Intermetall. (Bark.) 104 (2019) 113–123, https://doi.org/10.1016/j.intermet.2018.10.024.

[59] A. Pröschel, M.Lun Lau, D. Post Guillen, D.C. Dunand, Combining direct ink writing with reactive melt infiltration to create architectured thermoelectric legs, Chem. Eng. J. 479 (2024) 147845, https://doi.org/10.1016/J.CEJ.2023.147845.

[60] H. Park, C. Li, A.E. Jakus, R.N. Shah, H. Choe, D.C. Dunand, High-temperature mechanical properties of γ/γ′ Co–Ni–W–Al superalloy microlattices, Scr. Mater. 188 (2020) 146–150, https://doi.org/10.1016/j.scriptamat.2020.07.009.

[61] C. Xu, A. Bouchemit, G. L'Espérance, L. Laberge Lebel, D. Therriault, Solvent-cast based metal 3D printing and secondary metallic infiltration, J. Mater. Chem. C Mater. 5 (2017) 10448–10455, https://doi.org/10.1039/c7tc02884a.

[62] C. Xu, Q. Wu, G. L'Espérance, L.L. Lebel, D. Therriault, Environment-friendly and reusable ink for 3D printing of metallic structures, Mater. Des. 160 (2018) 262–269, https://doi.org/10.1016/J.MATDES.2018.09.024.

[63] M.M. Al Malki, G.J. Snyder, D.C. Dunand, Ink casting and 3D-extrusion printing of the thermoelectric half-Heusler alloy $Nb_{1-x}CoSb$, Addit. Manufact. Lett. 4 (2023) 100113, https://doi.org/10.1016/j.addlet.2022.100113.

[64] S. Peng, S. Mooraj, R. Feng, L. Liu, J. Ren, Y. Liu, F. Kong, Z. Xiao, C. Zhu, P. K. Liaw, W. Chen, Additive manufacturing of three-dimensional (3D)-architected CoCrFeNiMn high- entropy alloy with great energy absorption, Scr. Mater. 190 (2021) 46–51, https://doi.org/10.1016/j.scriptamat.2020.08.028.

[65] M.A. Skylar-Scott, S. Gunasekaran, J.A. Lewis, Laser-assisted direct ink writing of planar and 3D metal architectures, Proc. Natl. Acad. Sci. U.S.A. 113 (2016) 6137–6142, https://doi.org/10.1073/pnas.1525131113.

[66] C. Kenel, T. Davenport, X. Li, R.N. Shah, D.C. Dunand, Kinetics of alloy formation and densification in Fe-Ni-Mo microfilaments extruded from oxide- or metal-

powder inks, Acta Mater. 193 (2020) 51–60, https://doi.org/10.1016/j.actamat.2020.04.038.
[67] C. Kenel, N.P.M. Casati, D.C. Dunand, 3D ink-extrusion additive manufacturing of CoCrFeNi high-entropy alloy micro-lattices, Nat. Commun. 10 (2019) 1–8, https://doi.org/10.1038/s41467-019-08763-4.
[68] D. Zhang, C. Kenel, D.C. Dunand, Microstructure and mechanical properties of 3D ink-extruded CoCrCuFeNi microlattices, Acta Mater. 238 (2022) 118187, https://doi.org/10.1016/j.actamat.2022.118187.
[69] K.D. Koube, T. Sloop, C.D. Stiers, H. Sim, J. Kacher, Fabrication of 3D printed complex concentrated alloys using oxide precursors, Addit. Manufact. Lett. 1 (2021) 100015, https://doi.org/10.1016/j.addlet.2021.100015.
[70] M.A. Gianelle, C. Clapp, A. Kundu, H.M. Chan, Solid state processing of the cantor derived alloy CoCrFeMnNi by oxide reduction, Result. Mater. 14 (2022) 100286, https://doi.org/10.1016/j.rinma.2022.100286.
[71] T. Miyajima, K.-I. Yamamoto, M. Sugimoto, Effect of particle shape on packing properties during tapping, Adv. Powder Technol. 12 (2001) 117–134, https://doi.org/10.1163/156855201745001.
[72] P.Y. Wang, H.J. Li, L.H. Qi, X.H. Zeng, H.S. Zuo, Synthesis of Al-$TiAl_3$ compound by reactive deposition of molten Al droplets and Ti powders, Progr. Nat. Sci.: Mater. Int. 21 (2011) 153–158, https://doi.org/10.1016/S1002-0071(12)60049-5.
[73] N.R. Geisendorfer, R.N. Shah, Effect of polymer binder on the synthesis and properties of 3D-printable particle-based liquid materials and resulting structures, ACS Omega 4 (2019) 12088–12097, https://doi.org/10.1021/acsomega.9b00090.
[74] mmessers, https://www.thingiverse.com/thing:2138972, (n.d.).
[75] T. Dixit, E. Al-Hajri, M.C. Paul, P. Nithiarasu, S. Kumar, High performance, microarchitected, compact heat exchanger enabled by 3D printing, Appl. Therm. Eng. 210 (2022), https://doi.org/10.1016/j.applthermaleng.2022.118339.
[76] J.W. Yeh, S.K. Chen, S.J. Lin, J.Y. Gan, T.S. Chin, T.T. Shun, C.H. Tsau, S. Y. Chang, Nanostructured high-entropy alloys with multiple principal elements: Novel alloy design concepts and outcomes, Adv. Eng. Mater. 6 (2004) 299–303, https://doi.org/10.1002/adem.200300567.
[77] D.B. Miracle, O.N. Senkov, A critical review of high entropy alloys and related concepts, Acta Mater. 122 (2017) 448–511.
[78] E. Hong, B.Y. Ahn, D. Shoji, J.A. Lewis, D.C. Dunand, Microstructure and mechanical properties of reticulated titanium scrolls, Adv. Eng. Mater. 13 (2011) 1122–1127, https://doi.org/10.1002/adem.201100082.
[79] M.N. Rahaman, Kinetics and mechanisms of densification, in: Z.Z. Fang (Ed.), Sintering of Advanced Materials, Elsevier, 2010, pp. 33–64, https://doi.org/10.1533/9781845699949.1.33.
[80] F. Cabanettes, A. Joubert, G. Chardon, V. Dumas, J. Rech, C. Grosjean, Z. Dimkovski, Topography of as built surfaces generated in metal additive manufacturing: a multi scale analysis from form to roughness, Precis. Eng. 52 (2018) 249–265, https://doi.org/10.1016/J.PRECISIONENG.2018.01.002.
[81] S. Bagehorn, J. Wehr, H.J. Maier, Application of mechanical surface finishing processes for roughness reduction and fatigue improvement of additively manufactured Ti-6Al-4V parts, Int. J. Fatig. 102 (2017) 135–142, https://doi.org/10.1016/j.ijfatigue.2017.05.008.
[82] J.T. Black, R.A. Kohser, DeGarmo's Materials and Processes in Manufacturing, John Wiley & Sons, 2017.
[83] E. Maleki, S. Bagherifard, M. Bandini, M. Guagliano, Surface post-treatments for metal additive manufacturing: progress, challenges, and opportunities, Addit. Manuf. 37 (2021) 101619, https://doi.org/10.1016/j.addma.2020.101619.
[84] T. Persenot, A. Burr, R. Dendievel, J.Y. Buffière, E. Maire, J. Lachambre, G. Martin, Fatigue performances of chemically etched thin struts built by selective electron beam melting: experiments and predictions, Material. (Oxf.) 9 (2020) 100589, https://doi.org/10.1016/J.MTLA.2020.100589.
[85] D. Greitemeier, C. Dalle Donne, F. Syassen, J. Eufinger, T. Melz, Effect of surface roughness on fatigue performance of additive manufactured Ti–6Al–4V, Mater. Sci. Technol. (U.K.) 32 (2016) 629–634, https://doi.org/10.1179/1743284715Y.0000000053.
[86] C. Ma, M.T. Andani, H. Qin, N.S. Moghaddam, H. Ibrahim, A. Jahadakbar, A. Amerinatanzi, Z. Ren, H. Zhang, G.L. Doll, Y. Dong, M. Elahinia, C. Ye, Improving surface finish and wear resistance of additive manufactured nickel-titanium by ultrasonic nano-crystal surface modification, J. Mater. Process. Technol. 249 (2017) 433–440, https://doi.org/10.1016/J.JMATPROTEC.2017.06.038.
[87] M.-H. Tsai, K.-C. Chang, J.-H. Li, R.-C. Tsai, A.-H. Cheng, A second criterion for sigma phase formation in high-entropy alloys, Mater. Res. Lett. 4 (2016) 90–95, https://doi.org/10.1080/21663831.2015.1121168.
[88] T.M. Pollock, R.D. Field, Chapter 63 Dislocations and high-temperature plastic deformation of superalloy single crystals. Dislocations in Solids, 2002, pp. 547–618, https://doi.org/10.1016/S1572-4859(02)80014-6.
[89] T.M. Pollock, S. Tin, Nickel-based superalloys for advanced turbine engines: chemistry, microstructure and properties, J. Propuls. Power 22 (2006) 361–374, https://doi.org/10.2514/1.18239.
[90] J. Sato, T. Omori, K. Oikawa, I. Ohnuma, R. Kainuma, K. Ishida, Cobalt-base high-temperature alloys, Science (1979) 312 (2006) 90–91.
[91] A. Manzoni, S. Haas, H. Daoud, U. Glatzel, C. Förster, N. Wanderka, Tensile behavior and evolution of the phases in the $Al_{10}Co_{25}Cr_8Fe_{15}Ni_{36}Ti_6$ compositionally complex/high entropy alloy, Entropy 20 (2018) 646, https://doi.org/10.3390/e20090646.
[92] A.M. Manzoni, S. Haas, J.M. Yu, H.M. Daoud, U. Glatzel, H. Aboulfadl, F. Mücklich, R. Duran, G. Schmitz, D.M. Többens, S. Matsumura, F. Vogel, N. Wanderka, Evolution of γ/γ' phases, their misfit and volume fractions in $Al_{10}Co_{25}Cr_8Fe_{15}Ni_{36}Ti_6$ compositionally complex alloy, Mater. Charact. 154 (2019) 363–376.
[93] R. Völkl, U. Glatzel, M. Feller-Kniepmeier, Measurement of the lattice misfit in the single crystal nickel based superalloys CMSX-4, SRR99 and SC16 by convergent beam electron diffraction, Acta Mater. 46 (1998) 4395–4404, https://doi.org/10.1016/S1359-6454(98)00085-8.
[94] C.H. Zenk, S. Neumeier, H.J. Stone, M. Göken, Mechanical properties and lattice misfit of γ/γ' strengthened Co-base superalloys in the Co-W-Al-Ti quaternary system, Intermetall. (Bark.) 55 (2014) 28–39, https://doi.org/10.1016/j.intermet.2014.07.006.
[95] B.L. Bramfitt, The effect of carbide and nitride additions on the heterogeneous nucleation behavior of liquid iron, Metallurg. Transact. 1 (1970) 1987–1995, https://doi.org/10.1007/BF02642799.
[96] H. Biermann, M. Strehler, H. Mughrabi, High-temperature measurements of lattice parameters and internal stresses of a creep-deformed monocrystalline nickel-base superalloy, Metallurg. Mater. Transact. A 27 (1996) 1003–1014, https://doi.org/10.1007/BF02649768.
[97] Y. Yesilcicek, S. Haas, P. Suárez Ocaño, E. Zaiser, R. Hesse, D.M. Többens, U. Glatzel, A.M. Manzoni, Controlling lattice misfit and creep rate through the γ' cube shapes in the $Al_{10}Co_{25}Cr_8Fe_{15}Ni_{36}Ti_6$ compositionally complex alloy with Hf and W additions, High Entropy Alloy. Mater. (2022), https://doi.org/10.1007/s44210-022-00009-1.
[98] S. Haas, A.M. Manzoni, F. Krieg, U. Glatzel, Microstructure and mechanical properties of precipitate strengthened high entropy alloy $Al_{10}Co_{25}Cr_8Fe_{15}Ni_{36}Ti_6$ with additions of hafnium and molybdenum, Entropy 21 (2019) 169, https://doi.org/10.3390/e21020169.
[99] P.R. Strutt, R.S. Polvani, J.C. Ingram, Creep behavior of the heusler type structure alloy Ni_2AlTi, Metallurg. Transact. A 7 (1976) 23–31, https://doi.org/10.1007/BF02644035.
[100] Special Metals Company, INCONEL ® alloy 617, n.d. http://www.specialmetals.com/documents/Inconel%20alloy%20617.pdf (accessed December 10, 2023).
[101] A. Munitz, S. Salhov, S. Hayun, N. Frage, Heat treatment impacts the microstructure and mechanical properties of AlCoCrFeNi high entropy alloy, J. Alloy. Compd. 683 (2016) 221–230, https://doi.org/10.1016/J.JALLCOM.2016.05.034.
[102] Z. Wu, H. Bei, G.M. Pharr, E.P. George, Temperature dependence of the mechanical properties of equiatomic solid solution alloys with face-centered cubic crystal structures, Acta Mater. 81 (2014) 428–441, https://doi.org/10.1016/J.ACTAMAT.2014.08.026.
[103] J.J. Licavoli, M.C. Gao, J.S. Sears, P.D. Jablonski, J.A. Hawk, Microstructure and mechanical behavior of high-entropy alloys, J Mater Eng Perform 24 (2015) 3685–3698, https://doi.org/10.1007/s11665-015-1679-7.
[104] A.V. Kuznetsov, D.G. Shaysultanov, N.D. Stepanov, G.A. Salishchev, O.N. Senkov, Tensile properties of an AlCrCuNiFeCo high-entropy alloy in as-cast and wrought conditions, Mater. Sci. Eng.: A 533 (2012) 107–118, https://doi.org/10.1016/j.msea.2011.11.045.
[105] M.F. Ashby, Materials Selection in Mechanical Design, Butterworth-Heinemann, 2011.